Applied Thermal Engineering 128 (2018) 684–695

Contents lists available at ScienceDirect

Applied Thermal Engineering

journal homepage: www.elsevier.com/locate/apthermeng

Research Paper

Efficiency of water spraying on a heat exchanger: Local characterization with the impacted surface

P.E. Vende *, F. Trinquet, S. Lacour, A. Delahaye, L. Fournaison

Irstea, UR GPAN, 1 rue Pierre-Gilles de Gennes, 92761 Antony, France

HIGHLIGHTS

- Heat transfer enhancement of water spraying is higher at low surface temperature.
- A thermal image analysis is used to assess the efficient cooling surface.
- The efficient cooling surface is relevant to water spraying efficiency evaluation.
- The impacted surface depends on the surface temperature, not on the air flow.
- Spraying efficiency strongly depends on the local water-to-air mass flux ratio.

ARTICLE INFO

Article history:
Received 1 June 2017
Revised 7 August 2017
Accepted 7 September 2017
Available online 9 September 2017

Keywords:
Spraying efficiency
Efficient cooling surface
Atomizer position
Thermal image analysis
Water-to-air mass flux ratio

ABSTRACT

Due to climate change, worldwide power consumption for air conditioning is forecasted to increase by 33 times its current level by 2100. To face this trend, the efficiency of air conditioning and refrigeration systems must increase. Water spraying on the condenser of a refrigeration unit is one solution to reach this aim. Indeed, spraying water on a heat exchanger improves heat transfer by adiabatic cooling or direct impact on the heat-exchanger surface.

In the present paper, water spraying is designed for an embedded air conditioning application. A pilot designed for air conditioning conditions was built and equipped with a set of atomizer. The results obtained with this pilot show that heat transfer enhancement is higher at low heat exchanger surface temperature. Moreover, a thermal image analysis has highlighted that the surface impacted by the spray excluding the clogged parts is appropriate to express the local efficiency of the spray. Indeed, this surface reaches a steady-state approximately after the same time than heat transfer enhancement. This surface depends on heat-exchanger surface temperature, and not on the air flow. Finally, the efficiency of water spraying on a heat exchanger is correlated with the impacted surface.

© 2017 Elsevier Ltd. All rights reserved.

1. Introduction

Cooling applications is expected to overtake the current heating consumption by 2060 [1]. Moreover, worldwide power consumption for air conditioning is forecasted to increase by 33 times the current level by 2100 due to climate change and urbanization [2]. Increasing the efficiency of air conditioning and refrigeration systems is a way to reduce the energy consumption. In this end, system efficiency can be increased by spraying water on the condenser of a refrigeration unit.

Water sprays have become critical for many engineering process and industrial applications such as chemical protection against hazardous gases [3], fire protection [4], medical treatment [5], food preservation [6], surfaces cleaning [7], steel industry [8] or improving HVAC systems efficiencies by air cooling [9]. Indeed, water spraying water on a heat exchanger improves heat transfer in 2 ways. First, spray evaporates in the air and decreases the air temperature by adiabatic cooling process. Second, spray impacts the heat exchanger surface and increases the heat exchange coefficient thanks to the combination of a water film formation and water evaporation on the surface.

Interestingly, water spraying as a solution to enhance heat exchanger efficiency was generated by pioneers works [10,11] in the late 1950s and early 1960s. Elperin [11] reported a 30 times increase of the heat transfer with single-phase air heated tube bank by introducing water spray into the cooling air stream. Since then, a number of investigations have been carried out to understand more clearly the mechanisms involved in this kind of heat transfer. Nakayama et al. [12] obtained heat transfer and pressure

* Corresponding author.
E-mail address: pierre-emmanuel.vende@irstea.fr (P.E. Vende).

http://dx.doi.org/10.1016/j.applthermaleng.2017.09.031
1359-4311/© 2017 Elsevier Ltd. All rights reserved.

Nomenclature

Q	heat flux (W)
A	exchange surface (m^2)
$\dot{m}$	flow rate ($kg \cdot s^{-1}$)
v	flow velocity ($m \cdot s^{-1}$)
T	temperature (°C)
φ	humidity ($kg_w \cdot kg_a^{-1}$)
H	enthalpy ($J \cdot kg^{-1}$)
t	time (s)
Cp	heat capacity ($J \cdot kg^{-1} \cdot K^{-1}$)
C	heat capacity rate ($W \cdot K^{-1}$)
h	heat transfer coefficient ($W \cdot m^{-2} \cdot K^{-1}$)
ε	heat exchanger effectiveness (dimensionless)
σ	surface efficiency (dimensionless)
UA	overall thermal conductance ($W \cdot K^{-1}$)
Re	Reynolds number (dimensionless)
Pr	Prandtl Number (dimensionless)
Nu	Nusselt Number (dimensionless)
f	friction factor (dimensionless)
j	colburn factor (dimensionless)
μ	dynamic viscosity ($kg \cdot m^{-1} \cdot s^{-1}$)
ρ	density ($kg \cdot m^{-3}$)
k	thermal conductivity ($W \cdot m^{-1} \cdot K^{-1}$)
L_v	latent heat of vaporization ($J \cdot kg^{-1}$)
θ	louver angle (°)
l	length (m)
s	height (m)
w	depth (m)
λ	pitch (m)
δ	thickness (m)
Dh	hydraulic diameter (m)
x	horizontal position of the nozzle (cm)
y	nozzle-to-heat exchanger distance (cm)
z	vertical position of the nozzle (cm)
α	nozzle angle to the horizontal (°)
β	nozzle angle to the vertical (°)
N	number of items or configurations
Γ	local fluids flow rate ratio ($kg_w \cdot kg_a^{-1}$)
π	air-side spraying efficiency (dimensionless)
η	water-side spraying efficiency (%)
S	air permeability section (m^2)
τ	evaporation rate (%)
$\dot{m}''$	mass flux ($kg \cdot m^{-2} \cdot s^{-1}$)

Subscripts

hex	heat exchanger
a	air
w	water
i	inlet
o	outlet
Ps	pass
Tu	tube
Ch	channel
Lo	louver
Fi	fin
Al	aluminum
nz	nozzle
min	minimum
max	maximum
r	ratio
wet	wet
dry	dry
b	pass index
lam	laminar
turb	turbulent

drop data for smooth tubes, microfinned tubes and finned tubes with air velocity and water mass flux in the range of 1–3 $m \cdot s^{-1}$ and 50–390 $kg \cdot m^{-2} \cdot h^{-1}$, respectively. Authors obtained a heat transfer enhancement of 300–500% without increasing pressure drop. Dreyer et al. [13] have developed a mathematical model to analyze the spray-cooled finned-tube heat-exchangers. The proposed model was validated using experimental data and found a performance enhancement up to 3.5 times the dry performance with water mass flux that ranged between 250 and 450 $kg \cdot m^{-2} \cdot h^{-1}$. However, authors observed a significant increase in the pressure drop from 250 Pa to 500 Pa at air velocity of 9 $m \cdot s^{-1}$. Hasan [14] compared heat transfer enhancement of water spraying on plain circular tubes and on plate-finned tubes. The author observed an increase in heat transfer of about 92–140% for the plate finned tubes with air velocities from 1.66 to 3.57 $m \cdot s^{-1}$ and water mass flux of 1.78 $kg \cdot m^{-2} \cdot s^{-1}$.

Like most of the studies conducted on water spraying on heat exchangers, the previous studies were carried out with circular copper finned-tube heat-exchangers. Few studies consider louver fin flat-tube heat-exchangers cooled by water spray. Yang and Clark [15] tested three automotive radiator cores with plain-finned, louvered and perforated surfaces. Authors found that heat transfer coefficient was improved by 45% at an air-side Reynolds number of 500 when injecting water at a flow rate of 7.7 $L \cdot h^{-1}$ (or 83 $kg \cdot m^{-2} \cdot h^{-1}$ with heat-exchanger frontal area of 30.5×30.5 cm^2). These effects tend to decrease as air-side Reynolds number increases. For instance, an improvement equal to 13% was stated at air-side Reynolds number of 7000. Yang and Clark observed that water spraying has no effect on friction loss: as a result, no additional pressure drop was created. Youbi-Idrissi et al. [16] developed a semi-local mathematical model and applied it to a refrigerating machine with an air cooled condenser. Authors used the air flow rate of 1.4 $kg \cdot s^{-1}$, water flow rate of up to 0.033 $kg \cdot s^{-1}$ (or 270 $kg \cdot m^{-2} \cdot h^{-1}$ and a condenser volume of $1.122 \times 0.398 \times 0.156$ m^3) and found that the machine COP could increase up to 55% compared to a dry air cooled condenser. Zhang et al. [17] developed a model of a spray cooled finned-tube heat exchanger partially wetted with air velocities from 1.8 to 3.2 $m \cdot s^{-1}$ and a water spray rate of up to 1.2 $g \cdot m^{-2} \cdot s^{-1}$(4.3 $kg \cdot m^{-2} \cdot h^{-1}$). Authors obtained a heat capacity enhancement thanks to water spraying up to 3 times, from 541 $W \cdot m^{-2}$ to 1582 $W \cdot m^{-2}$. Tissot et al. [18] carried out an experimental study on a heat exchanger cooled by a water spray in counter flow. The water spray rate was varied from 1.12 to 1.68 $L \cdot h^{-1}$ (12.4 to 18.7 $kg \cdot m^{-2} \cdot h^{-1}$), as well as the air velocity ranged between 1.1 and 2.2 $m \cdot s^{-1}$. Heat transfer enhancement up to 3 times was achieved when using a sprayed air flow upstream from the heat exchanger. Chen [19] investigated the effects of water spraying rate, air flow rate and relative humidity on the heat transfer performance of a flat aluminum tube microchannel heat exchanger. Author tested the air velocities from 0.8 to 5.3 $m \cdot s^{-1}$ and water spray flow rate between 0.5 and 2.5 $g \cdot s^{-1}$ (12.4 to 62 $kg \cdot m^{-2} \cdot h^{-1}$). As a result, the heat transfer performance was enhanced up to 21% at a lowest spraying rate of 12.4 $kg \cdot m^{-2} \cdot h^{-1}$ with a low Reynolds number range (<350). The results thus suggested that higher spray rates enhance greatly the thermal performance but the friction penalties become an issue.

However, the few studies conducted about water spraying on a microchannel heat exchanger were performed with very fine spray

(droplet diameters less than 20 μm) injected at least at 20 cm away from the heat exchanger surface. In this case, it is assumed that all the droplets can evaporate before reaching the heat exchanger surface [20]. This ensures no water stagnation on the condenser that could leads into microbial organisms to appear or grow. Nevertheless, this spraying system is very energy consuming because water needs to be injected at high pressure (>30 bar) [21]. Moreover, authors rarely focus on the local effect of spraying assuming that the heat exchanger is entirely wet. But the spray rarely impacts all the surface of the heat exchanger, as detailed by Zhang [17]. Thus, the heat exchanger is partially wet between 20 and 60% depending on the water spray rate.

In the present study, the spray injected is coarser than usual (Sauter mean diameter of 50 μm) and closer to the heat exchanger (about 5 cm) in order to get the smallest and most energy efficient spraying system for an embedded air conditioning application. Moreover, the frontal area of the heat exchanger is large and water spray will impact only partially the heat exchanger. A previous paper from the same authors [22] initiated a discussion regarding the possible influence of the atomizer position and the impacted surface on the efficiency of the heat transfer. The present work has further examined those questions by new measurements. The novelty of this research is to study the local effect of water spraying regarding the global efficiency and to better understand the heat transfer enhancement by wetting the heat exchanger. This local effect of water spraying is characterized by a new method of thermal image analysis that gives the time evolution of the impacted surface. The effects of water spraying rate, air flow rate, wall temperature and nozzle position on the heat transfer and the impacted surface are discussed.

2. Material and method

2.1. Experimental devices

The purpose of the experiment is to characterize the efficiency of water spraying on a heat exchanger. The effects of operating parameters such as air flow, water flow and nozzle position on the global efficiency are evaluated. The experimental set up is described on Fig. 1.

The device is located in a climatic room where the temperature and humidity are controlled. It is composed of 3 main parts, the heat exchanger, the air flow and the spraying system. The heat exchanger is a four-pass flat-tube condenser made in aluminum. The numbers of channels for each pass were 16, 12, 8 and 6, respectively from the top to the bottom. Heat exchanger dimensions are shown in the Table 1 below.

Circulation of water in the exchanger is assured by a 10 kW temperature control unit Vulcatherm 10805. The inlet water temperature varies from 10 to 110 °C and the inlet water flow rate goes up to 550 $L{\cdot}h^{-1}$. The air flow through the heat exchanger with a help of a fan located downstream the exchanger. The flow rate was set from 450 to 900 $kg{\cdot}h^{-1}$. The spraying system is composed of an atomizer, a 15 L bottle of water and a pump. The pump brings water from the bottle to the atomizer that pulverizes it into a spray. Pump pressure was adjusted at 5 and 10 bar. These pressures correspond to water flow rates of 1 $L{\cdot}h^{-1}$ and 1.4 $L{\cdot}h^{-1}$, respectively depending on the amount of water obtained at the evaporator of the same refrigeration unit [22]. Spray atomization was achieved with hollow cone nozzles (LECHLER type 212.014) equipped with 0.15 mm diameter hole. This spray produces a droplet size distribution with a Sauter diameter of 64 and 49 μm for respectively 5 and 10 bar pump pressure. These values were obtained by PDA measurements (Dantec Dynamics, with a volume measurement of 189 μm and a time resolution of 0.1 μs).

The nozzle locations on the condenser are described in Fig. 2. There are three main choices for the atomizer orientation: in co-flow, in counter-flow and perpendicular to the air flow. The co-flow orientation gives poor results because the spray impacts a very small surface due to the short distance between the nozzle and the condenser. The second option, the counter flow orientation is more efficient as the droplets have longer time to evaporate and spread in the air [23–25]. Nevertheless, this option takes too much space in regard to the application and cannot be adopted. Finally, the perpendicular orientation appears as a good compromise. In this study, 8 configurations were perpendicular to the air flow and 3 configurations have an angle of 45° with the condenser. This angle was chosen purposely to have a longer evaporation time in order to compare with the perpendicular configurations. Fig. 2 gives more details about the 11 nozzle positions. Since the atomizer must disturb slightly the air flow passing through the exchanger, therefore nozzles were located on the edge of the condenser. For each trial, one nozzle was set on the condenser.

2.2. Measurements

On the water side, an electromagnetic flow-meter measures the flow rate in the heat exchanger and two Pt100 measure the inlet

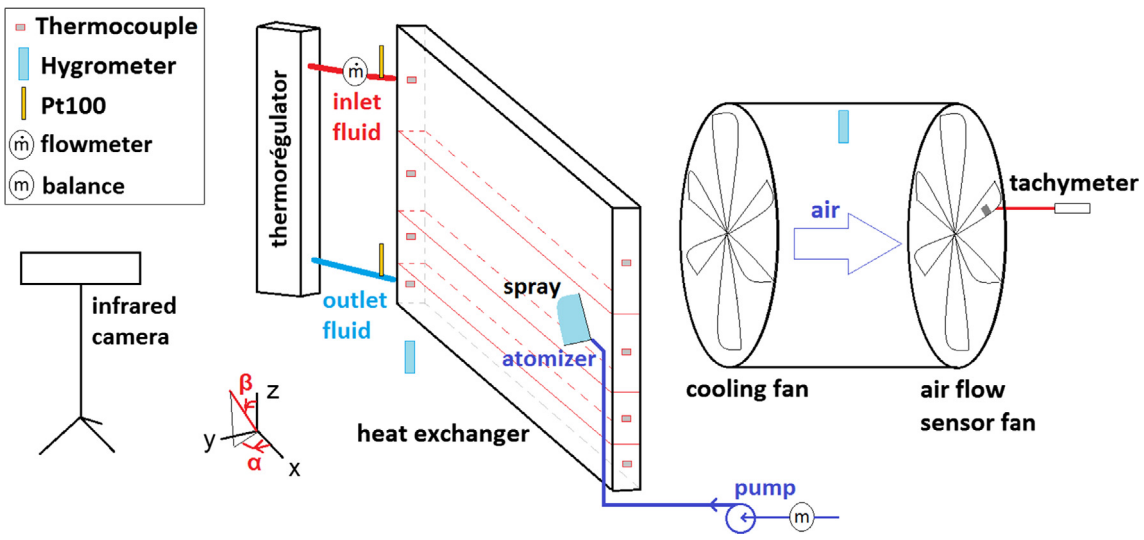

Fig. 1. Schematic representation of the experimental device.

Table 1
Detailed dimensions of the condenser.

Heat exchanger width l_{hex} (mm)	513	Fin pitch λ_{Fi} (mm)	1.1
Heat exchanger height s_{hex} (mm)	396	Fin thickness δ_{Fi} (mm)	0.07
Number of tubes N_{Tu}	42	Louver pitch λ_{Lo} (mm)	1.0
Number of channel for each tube N_{Ch}	5	Louver length l_{Lo} (mm)	6.32
Frontal area $l_{hex} \times s_{hex}$ (m^2)	0.203	Louver angle θ (°)	20
Air permeability section S (m^2)	0.153	Tube pitch λ_{Tu} (mm)	9.17
Fin depth w_{Fi} (mm)	12	Tube thickness δ_{Tu} (mm)	0.35
Fin length l_{Fi} (mm)	7.42	Tube height s_{Tu} (mm)	1.75

and outlet temperatures. The air flow passing through the heat exchanger was measured using air flow sensor fan. The rotation frequency was assessed by a tachymeter and a calibration curve made previously with a Pitot tube that provides the air flow measurement. Two sensors measure the humidity and temperature upstream and downstream the heat exchanger. The nozzle water flow-rate was obtained by the time derivative of the water mass contained in the bottle. The data was recorded with a data logger (Agilent National Instrument) in every 10 s. An infrared camera measures the surface temperature of the heat exchanger at pixel resolution of the image of 320 × 240. The uncertainties of the experimental apparatus used are reported in table 2.

2.3. Protocol

Two kinds of experiment framework were carried out as described below: the first set of trial was performed to evaluate the impact of the nozzle location on the global efficiency of the heat exchanger. While, the second one was designed to focus on determining the relation between the surface impacted and the efficiency of the heat exchanger. Both frameworks ran at air flow rates of 450 to 900 kg·h^{-1}, which correspond to the extreme operating conditions of the cooling fan.

For the first set of experiment, the 11 nozzles were tested separately. The inlet water temperature was set at 80 °C and the water flow rate in the heat exchanger at 200 L·h^{-1}. The two pump pressures for spraying were 5 and 10 bar. The infrared camera was placed at 2 m away from the heat–exchanger surface. 5 pixels correspond to 1 cm in both directions (25 pixels/cm^2).

For the second set of experiment, the measurement of the impacted surface by the spray was made in one location of the nozzle on the heat exchanger. The water flow rate in the heat exchanger was set at 520 L·h^{-1} with different water inlet temperatures of 40, 50 and 70 °C. Five air flow rates were studied: 450, 520, 580, 700 and 900 kg·h^{-1}. The pump pressure was set at 10 bar, which delivers a water mass flow rate of 1.4 L·h^{-1}. Here, the infrared camera was placed closer to the heat exchanger at 1.1 m to have a better contrast, and under this configuration, 9 pixels correspond to 1 cm in both directions (81 pixels/cm^2).

Table 3 presents the details of the experimental parameters.

Each experiment takes about one hour. Fig. 3 describes the experimental procedure. A steady state was obtained without spraying for one air flow rate and one pump pressure. After about 5 min the spraying was switched on, and the water outlet temperature decreased immediately, as well as the downstream air temperature. The cycling variation of the water temperatures at the inlet was due to the heat/cool mode of the temperature control unit. Air temperature stabilizes after about 5 min, when a steady state is reached. After 5 min of the stabilization period, the spraying was stopped and the outlet water temperature returns to its previous level, as well as the outlet air temperature. The next experiment was then implemented after 30 min to leave the heat-exchanger to dry in order to have the same steady state before spraying.

During the test, pictures were taken with the Infrared camera, one before spraying and at least five images during spraying to have a minimum of one image every two minutes. A flowchart of the experimental procedure from start step to end step is given in Appendix B.

2.4. Data analysis of the system efficiency

The spraying influences on the system efficiency was studied globally for the different air flows, sprayed water flows, inlet heat-exchanger's water temperature, nozzle position and orientation. The following section defines the key parameters for the data analysis.

The system efficiency was characterized based on the ε-NTU method with the Colburn factor. This factor [26] is a dimensionless representation of the heat transfer coefficient of the studied fluid (air) and is proportional to the NTU of the fluid.

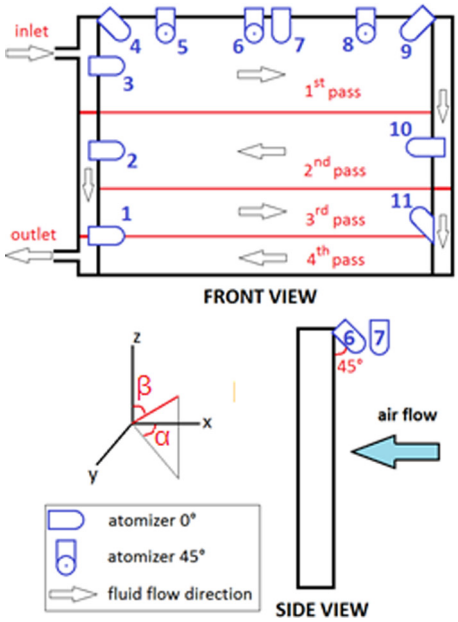

N_{nz}	x (cm)	y (cm)	z (cm)	α (°)	β (°)
1	0	4	8	0	90
2	0	4	18.5	0	90
3	0	4	34	0	90
4	0	6	30.5	0	135
5	11	5.5	37	90	135
6	24	7	38.5	90	135
7	24	5	37.5	90	180
8	40	7	37	90	135
9	52	5	34	180	135
10	52	3.5	18.5	0	90
11	52	5	15	180	45

Fig. 2. Nozzle positions and orientations on the heat exchanger.

Table 2
Measurement type, apparatus and uncertainties.

Measurement	Apparatus reference	Measurement range	Accuracy
Water flow rate (heat exchanger)	Flowmeter Endress& Hauser Promag 50H	0 > 600 $m^3 \cdot h^{-1}$	±0.5%
Air flow rate	Tachymeter ALMEMO ref : FUA9192	8 > 30,000 trs·min^{-1} 600 trs·min^{-1} ≈ 500 kg·h^{-1}	±0.02%
Water injected pressure	Pressure sensor RS ref : 797–4995	0 > 100 bar	±0.25%
Weighting of water supply	Scale Mettler ref : PE24	0 kg > 24 kg	±2 g
Air, Water & Wall temperatures	Thermocouple TCSA Type T ref : B10-TX	−75 °C > 250 °C	±0.1 °C (calibrated)
Inlet & Outlet fluid temperatures	Pt100 Prosensor	−50 °C > 250 °C	±0.1 °C
Humidity	Hygrometer Vaisala ref : HMP110	0 > 100% −40 > 80 °C	RH: ± 1.1% 0 > 90%; ±1.8% 90 > 100% T : ± 0.2 °C
Impacted surface	Infrared camera Ref :ThermaCAM FLIR E45	Resolution: 320 × 240 px 5 px = 1 cm	±20%

Table 3
Experimental parameters.

Inlet air temperature	Inlet air relative humidity	Inlet heat-exchanger water temperature	Inlet heat-exchanger water flow rate	Air flow rates	Water spray flow rates
30 °C	28%	40, 50, 70 °C	200, 520 L·h^{-1}	450, 520, 580, 700, 900 kg·h^{-1}	1.0, 1.4 L·h^{-1}

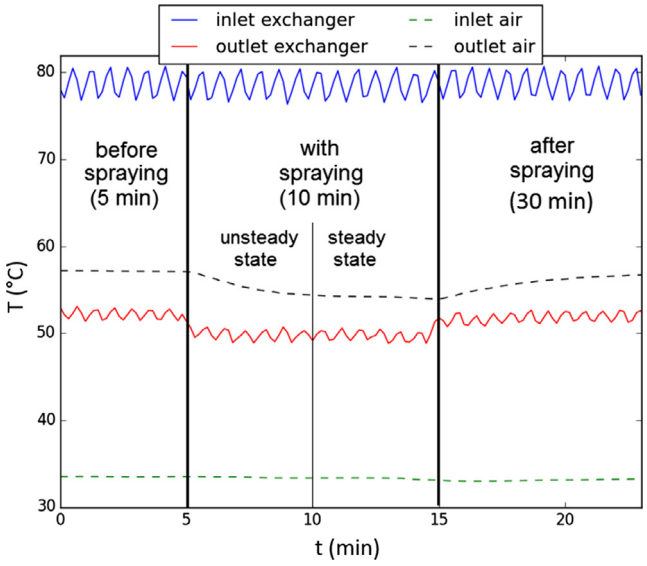

Fig. 3. Typical evolution of inlet/outlet air and exchanger temperatures (atomizer 6, T_i^{hex} = 80 °C, $\dot{m}_w^{hex}$ = 200 L·h^{-1}, $\dot{m}_w^{nz}$ = 1.4 L·h^{-1} and $\dot{m}_a$ = 450 kg·h^{-1}).

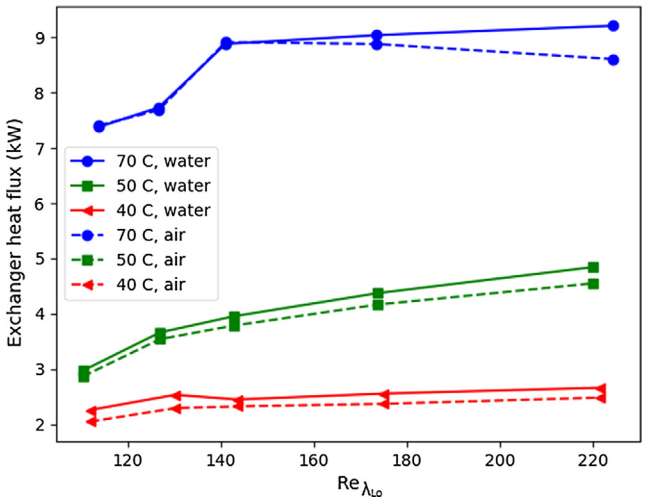

Fig. 4. Air side and water side heat transfer rate for the second set of tests (T_i^{hex} = 40, 50 and 70 °C, $\dot{m}_w^{hex}$ = 500 L·h^{-1}, $\dot{m}_a$ = 450, 520, 580, 700 and 900 kg·h^{-1}).

The heat transfer flux of the heat exchanger on the air-side and water-side is first determined for all the operating conditions using Eqs. (1) and (2):

$$Q_w^{hex} = \dot{m}_w^{hex} Cp_w (T_{wi}^{hex} - T_{wo}^{hex}) \quad (1)$$

$$Q_a^{hex} = \dot{m}_a (H_{ao} - H_{ai}) \quad (2)$$

With,

$$H_a = Cp_{a,dry} T_a + \phi (L_v + Cp_{a,w} T_a) \quad (3)$$

Fig. 4 represents the heat exchanged both on the air and water side as a function of the air-side Reynolds number $Re_{\lambda_{Lo}}$ (Eq. (5)), for the three water inlet temperatures of 40, 50 and 70 °C. These preliminary results were obtained without spraying. The discrepancy between the heat fluxes on the water side and the air side was small, of about 6%. However, a divergence for higher temperature and flow rates is observed, because the air sensors were located far from the heat exchanger surface (at 20 cm) due to space issue. Thus, heat fluxes for air were underestimated relative to those for water because air temperatures were too low, especially downstream the heat exchanger. Based on this discrepancy, the heat flux in this work was considered to be always related to the water side. The increase of the air flow rates increases the heat flux in the exchanger.

The air-side Reynolds number $Re_{\lambda_{Lo}}$ was computed using the air density ρ_a, dynamic viscosity μ_a at the inlet air temperature T_{ai} and the air velocity v_a, assuming uniform on all the heat-exchanger frontal area. v_a was calculated as the ratio of the measured air flow rate $\dot{m}_a$ on the air permeability section S (heat-exchanger frontal area without tubes and fins, expressed in Eq. (4)) and the louver pitch λ_{Lo} as characteristic length). This choice was implemented as proposed by the work of Chen [19] and Zhang [17].

$$S = l_{hex}(s_{hex} - (N_{Tu} + 2)s_{Tu} - \frac{(N_{Tu} + 1) l_{Fi} \delta_{Fi}}{\lambda_{Fi}}) \quad (4)$$

$$Re_{\lambda_{Lo}} = \frac{\rho_a v_a \lambda_{Lo}}{\mu_a} \quad (5)$$

From the ε-NTU method, the heat transfer rate was expressed as Eq. (6):

$$Q^{hex} = \varepsilon C_{min}(T_{wi}^{hex} - T_{ai}) \quad (6)$$

The Number of Transfer Unit (NTU) was determined from the heat exchanger efficiency ε based on the ε-NTU relation from Kays and London [27]:

$$\varepsilon = 1 - \exp\left(\frac{1}{C_r}[\exp(-C_r \cdot NTU) - 1]\right) \quad (7)$$

With,

$$C_r = \frac{C_{min}}{C_{max}}; \quad \begin{matrix} C_{min} = \min(m_a Cp_{a,wet}, \dot{m}_w^{hex} Cp_w) \\ C_{max} = \max(m_a Cp_{a,wet}, \dot{m}_w^{hex} Cp_w) \end{matrix}; \quad Cp_{a,wet} = \frac{H_{ai}}{T_{ai}}$$

With the NTU, the overall thermal conductance is deducted from the relation $UA = C_{min}NTU$.

By definition, the overall thermal conductance combines three kinds of heat transfers: the wall heat conduction, the water-side convection in the minichannels and the air-side convection through the heat exchanger. Thus the overall thermal conductance is:

$$\frac{1}{UA} = \frac{1}{\sigma_a h_a n A_a^{hex}} + \frac{\delta_{Tu}}{k_{Al} A_a^{hex}} + \frac{1}{h_w A_w^{hex}} \quad (8)$$

Between these three terms, only the water spraying was observed to influence the air-side convective term. Therefore, the other terms in Eq. (8) were as details in the Appendix A.

Finally, the Colburn factor is determined from the air-side heat transfer coefficient h_a using Eq. (9).

$$j = \frac{h_a}{\rho_a v_a Cp_a} Pr_a^{2/3} \quad (9)$$

The Colburn factor can be calculated in dry and wet conditions. The air-side spraying efficiency, called π, can be expressed by the ratio of the Colburn factors and defined by using Eq. (10):

$$\pi = \frac{j_{wet}}{j_{dry}} \quad (10)$$

2.5. Thermal images analysis

Thermal images were obtained with the infrared camera during the experiments. These images show the temperature distribution on the exchanger surface. Fig. 5 displays a set of pictures taken at different time that represents evolution of the impacted surface. At first, the pictures without spraying were taken (t = 0). This measurement shows that the temperature decrease in the 4 passes of the heat exchanger. This image was considered as the reference image of the heat exchanger in given operating conditions. Once water spraying begins, the surface temperature decreases on the small area impacted by the spray. From picture t = 45 s to t = 10 min, the impacted area expands as some spots tend to warm up, whereas the shape of the area tends to extend downwards. The local rise of temperature was due to the fact that the exchanger locally clogs with the water drainage, which disables the air to pass through the exchanger. Besides, the impacted surface shape changes and the stain rises at its bottom, while water runs-off because of the local clogging.

An image processing was carried out to define the impacted surface. The steps of the image processing are detailed next and represented in Fig. 6.

The first step consisted in subtracting the image of the heat-exchanger surface without spraying to the images with spraying. This procedure highlights the impacted surface. Then, the picture was converted into a greyscale histogram for further image analysis processes. After, a discrete Fourier transformation was applied. The Fourier transformation was multiplied by an appropriate mask (given in Fig. 6) allowing the parasite periodic signal of the heat exchanger tubes to be filtered. Then to go back to a real domain,

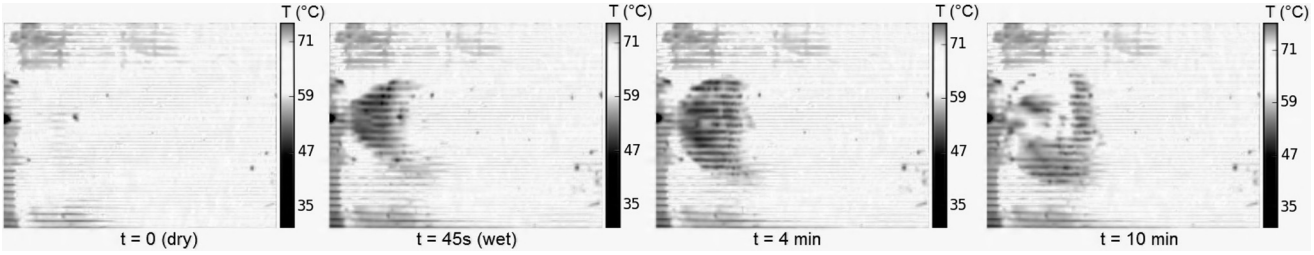

Fig. 5. Time evolution of thermal images at $T_i^{hex} = 70$ °C, $\dot{m}_w^{hex} = 500$ L·h^{-1}, $\dot{m}_w^{nz} = 1.4$ L·h^{-1} and $\dot{m}_a = 520$ kg·h^{-1}.

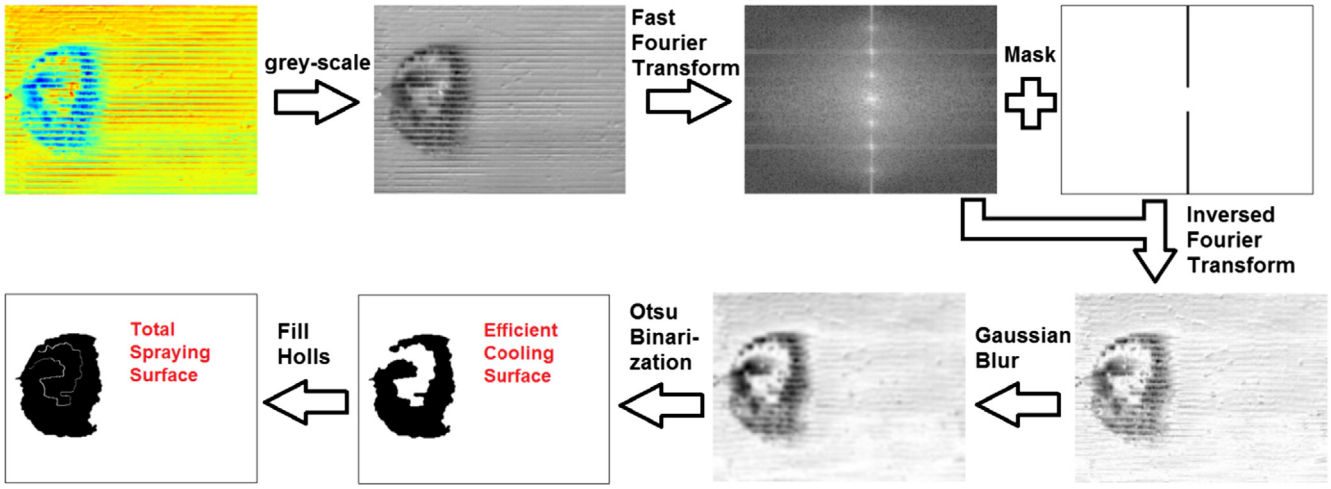

Fig. 6. Steps of the image processing.

the inverse Fourier transformation was applied. Later, Gaussian function was used to smooth the remaining noise in the images. Finally, the image was segmented by the Otsu's method. The method is based on discriminant analysis and tends to maximize the "between-class variance" of the greyscale level to offer the best separation of the regions of interest from the background. This allows an impacted surface to be separated by counting the number of pixels with non-zero values. In some cases, the obtained surface contained holes that correspond to the spots with a temperature rise, i.e. where the heat exchanger is clogged. To have the total surface impacted by the spray, these holes were filled using a pre-existing function available in Python.

This image processing provides two different values for the impacted surface by the spray. Indeed, a major surface difference appears while considering the entire area impacted by the spray (total spraying surface) or only the area where an efficient impact of the spray is obtained (efficient cooling surface). These two surfaces are respectively noted as $S_w^{nz,ec}$ and $S_w^{nz,ts}$. To validate the total spraying surface, the images were also analyzed using Image J 1.48v (National Institutes of Health, USA). The results are accurate at 10% showing the reliability of the algorithm.

3. Results and discussion

3.1. Influence of atomizer position

The water spraying efficiency was evaluated for this system and the influence of air flow, water flow injected and atomizer position are discussed.

The first set of experiments was implemented to estimate the influence of the atomizer position. For each position, the Colburn factor was determined in dry and wet conditions (without/with spraying) for both injected water pressures and air flow rates tested. As an example, Fig. 7 shows the Colburn factor obtained for the atomizer 11 in dry and wet conditions at 2 air flow rates of 450 and 900 kg·h^{-1} corresponding to the Reynolds numbers of 110 and 220.

The Colburn factor in dry and wet conditions decreased with the Reynolds number as it has been reported by several publications [28–30]. In dry condition, the Colburn factor was 0.035 and 0.030 at the Re = 110 (450 kg·h^{-1}) and the Re = 220 (900 kg·h^{-1}), respectively. This decrease behavior was due to a decrease in the fanning friction factor, that is to say, a decrease in the pressure drop relative to the air flow rate. Then, the same amount of air is less heated and so the air-side heat transfer coefficient improvement is not proportional to the air flow rate increase. For wet conditions, the Colburn factor was higher than in dry conditions, as water spraying induces a heat transfer gain. This gain increases also with the water flow – for the Re = 110, the Colburn factor in wet conditions was 16% higher than the same value in dry conditions at 1 L·h^{-1} injected water and 26% at 1.4 L·h^{-1}.

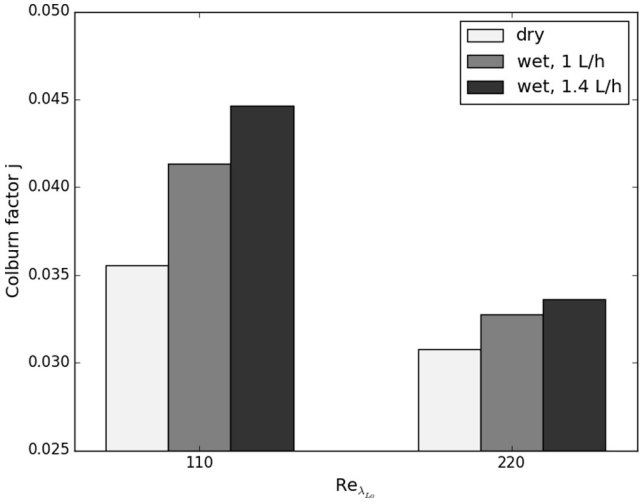

Fig. 7. Colburn factor under dry and wet conditions at two Reynolds number for the atomizer 11.

On the contrary, the Colburn factor enhancement decreases with the Reynolds number because the ratio of sprayed water to the air flow was observed to be smaller. These findings are consistent to the results in the literature [15,19,30,31]. However, the heat transfer enhancement was measured to be higher than the usual one of 21% at 1.8 L·h^{-1} for the Re < 350 as reported by Chen [19] at less water consumption. This analysis has been conducted for all the atomizer positions by representing air-side spraying efficiency π as a function of water-to-air-flow ratio as shown in Fig. 8.

Fig. 8a combines the data for atomizers 1, 2, 3, 7 and 10, which were horizontal (or vertical for 7) and orthogonal to the air flow. Fig. 8b shows the atomizers 4, 5, 8, 9 and 11 inclined at a 45° angle to the vertical or the horizontal plane. Furthermore, these atomizers are vertical with a 45° counter current orientation to the air flow (5, 8) or they are in the corners of the heat exchanger and oriented in diagonal orthogonal to the air flow (4, 9, 11). For all the atomizers position, the increase of sprayed water flow increases the π values as shown in Fig. 8. The air-side spraying efficiency depends on the position of the atomizer. For the atomizers without 45° angle, the π values of atomizers 3, 7 and 10 were lower than those of atomizer 1. This is due to the fact that atomizer 1 impacts the coldest surface of the heat exchanger (pass 3 and 4) while atomizers 3, 7 and 10 impact the hottest surface (pass 1 and 2). Therefore, the heat transfer enhancement was observed to be better when the wall temperature was lowered. However, atomizers 1 and 2 have the same efficiency at water/air ratio of 2 g·kg^{-1}. Indeed, for atomizer 1, the water sprayed partially drifts below the heat exchanger, unlike the atomizer 2 where the water sprayed drains over the pass 3 and 4 of the heat exchanger, and thus contributes to the cooling effect. This effect disappears when water flow increases because more water settles on the hot surface (pass 2) which is not as effective as on cold surface (pass 3 and 4). Consequently, the efficiency of atomizer 2 becomes similar to those of atomizers 3, 7 and 10.

For the atomizers with 45° angle, the π values were found to increase with the amount of water sprayed. Unlike the previous atomizers, where rise in both injected water pressure and water flow increase the distance travelled by the spray leads to a larger impacted surface. Thus, all the atomizers located near pass 1 (atomizers 4, 5, 8 and 9) impacts pass 1 and 2 without creating clogging or hot spots. Moreover, the quasi counter flow configurations represented (5, 8) were better than the corresponding perpendicular configuration (7).

The findings thus suggest that wall temperature influences strongly the water spraying efficiency on the heat exchanger.

However, according to Table 4, all the efficiencies obtained were poor compared to that obtained with a total evaporation of the sprayed water upstream the heat exchanger. In this table, the values correspond to the percentage of additional heat flux obtained with water spraying. These are the water-side spraying efficiencies η as in [22] and defined as:

$$\eta_{exp} = \frac{Q_{w,wet}^{hex} - Q_{w,dry}^{hex}}{Q_{w,dry}^{hex}} \tag{11}$$

$$\eta_{evap} = \frac{\dot{m}_w^{nz} L_v}{Q_{w,dry}^{hex}} \tag{12}$$

The efficiency η is introduced here because the heat exchanger outlet temperature drop caused by water spraying total evaporation is not known: consequently, the Colburn factor cannot be

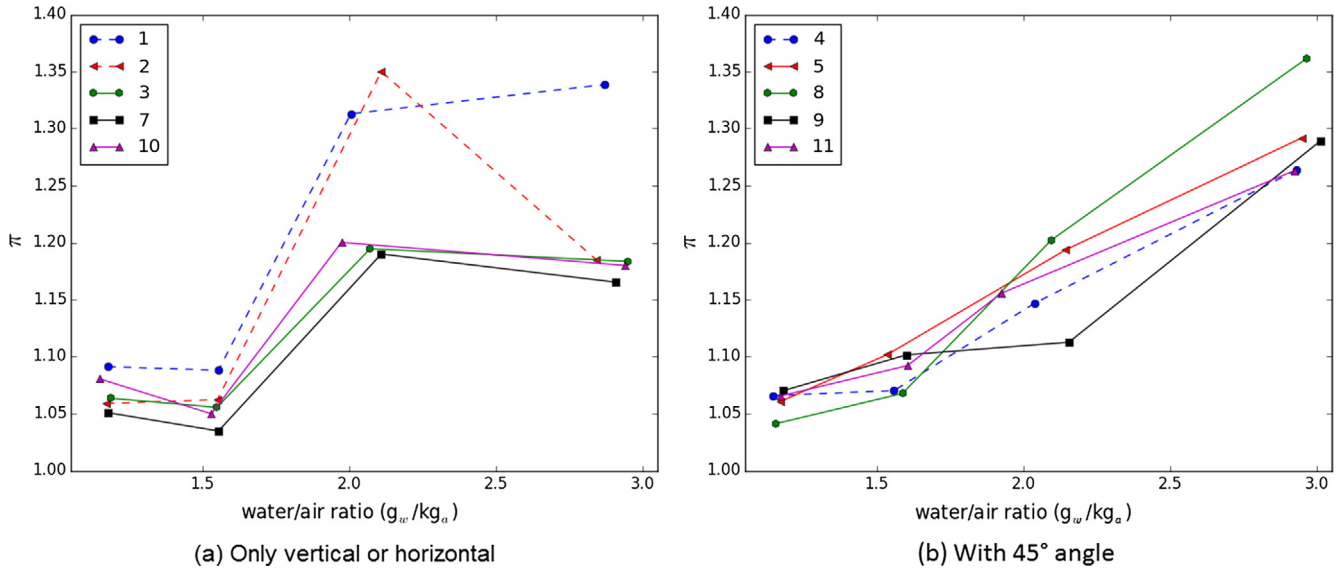

Fig. 8. Thermal efficiency of spraying vs water on air flow rate ratio for the different atomizer orientation tested.

Table 4
Water-side spraying efficiencies: experimental and with total evaporation.

$\dot{m}_a$ (kg·h^{-1})	$\dot{m}_w^{nz}$ (L·h^{-1})	π (%)	η_{exp} (%)	η_{evap} (%)
450	1.0	1.11– 1.35	2.6–6.4	11.0 ± 0,7
	1.4	1.16–1.36	4.3–8.0	15.5 ± 0.5
900	1.0	1.04–1.09	0.9–2.1	8.8 ± 0.3
	1.4	1.03–1.10	0.8–2.3	11.8 ± 0.3

properly calculated with Eq. (1). But, as the air-side and water-side spraying efficiencies π and η are proportional, the heat exchange on the water side is consistent for the analysis.

The comparison between η_{exp} and η_{evap} shows that the sprayed water was partially exploited. Indeed, the total evaporation values worth 2–4 times the experimental values at 450 kg·h^{-1} air flow rate and over 4 times at 900 kg·h^{-1} air flow rate. This difference can be explained by a poor evaporation rate, observed to be between 10 and 20% [22] in the experiments, because of the small distance between the nozzle and the exchanger surface. As the water droplets do not have enough time to evaporate almost all the water impacts the heat exchanger surface and creates a water film. Nevertheless, it was noticed that there is less difference between η_{exp} and η_{evap} for low air flow rate and sprayed water flow rate. This means that sprayed water was better exploited because this is the best compromise between water film evaporation and drainage produced by air flow and water film renewal caused by water flow. It seems that the impact surface has an influence on the global efficiency of the heat exchanger. In the next Section, a thermal images analysis is presented to characterize the impacted surface.

3.2. Impacted surface determination

The effects of air flow rate and wall temperature on the surface impacted by the spray were evaluated with the second set of tests. A focus on the atomizer 2 was carried out to study the influence of the operating parameters on the impacted surface of the heat exchanger. Atomizer 2 was chosen because it has the greatest range of π. The thermal image analysis aims to determine the effect of the air flow rate and the inlet heat exchanger temperature (and so the wall temperature) on the time evolution of the total spraying surface and the efficient cooling surface.

Fig. 9 outlines the time evolution of total spraying surface for the five air flow rates tested and with an inlet heat exchanger temperature of 50 °C. The results show that the five air flow rates have the same evolution in time (a continual rise) and very close values. Inspite the uncertainties of measurement, it is deduced that the air flow rate has very little influence on the total spraying surface. This result was reported also by Zhang [17] where the wetted area of the heat exchanger depends mainly on the water spray flow-rate, unlike on the air flow rate. On one hand, the wetted area increases from 20% to 60% when the water spray rate ranges from 0.2 to 1 kg·m^{-2}·s^{-1} respectively. Besides, the wetted area values were similar with the uncertainties, for air velocity between 1.8 m·s^{-1} and 3.2 m·s^{-1}.

Concerning the influence of wall temperature on the total spraying surface, Fig. 10 shows the time evolution of the total spraying surface for the three water inlet temperatures for all air flow rates. The results show that the total spraying surface increases quickly when the wall temperature is lowered. In this case, the water film evaporates slowly, thus induces more clogging and so more drainage, which increases the total spraying surface.

Fig. 9 and Fig. 10 show the total spraying surface that increases continuously with time. However, it was noticed that the heat exchanger outlet temperature stabilizes in less than 2 min as delineated in Fig. 3. This means that the maximum heat transfer enhancement was reached quickly, although the total spraying surface increases. Therefore, it can be considered that the total spraying surface was inaccurate parameter to evaluate the spraying efficiency.

The efficient cooling surface was studied carefully as represented in Fig. 11. Similarly to the total spraying surface, the efficient cooling surface was noticed to be independent from the air flow rate. This surface reaches a maximum after nearly 200 s which is consistent with the behavior shown in Fig. 3. Also, the efficient cooling surface depends on the heat exchanger inlet temperature and consequently on the wall temperature. When the wall temperature decreases, the efficient cooling surface increases. At the steady-state, it represents 185 cm^2 at 40 °C, 170 cm^2 at 50 °C and 140 cm^2 at 70 °C. These are less than 10% of the front area (2031 cm^2) and less than the 20–60% as reported by Zhang [17].

The efficient cooling surface was relevant to evaluate the spraying efficiency, as this surface reaches a steady-state approximately after the same time than the outlet temperature of the heat exchanger in Fig. 3.

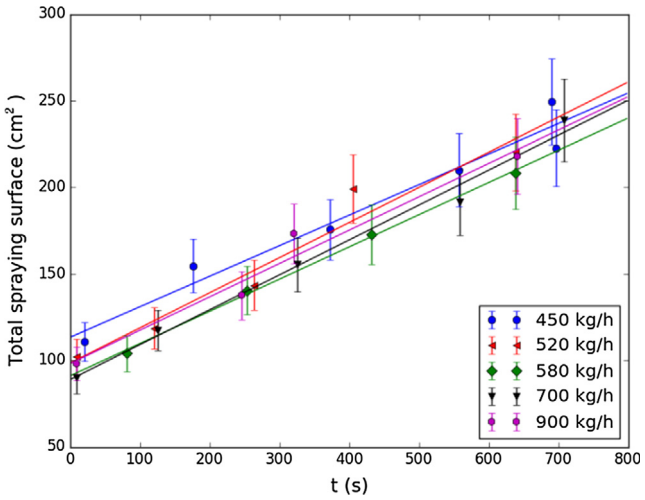

Fig. 9. Time evolution of the total spraying surface at $T_i^{hex} = 50$ °C, $\dot{m}_w^{hex} = 500$ L·h^{-1}, $\dot{m}_w^{nz} = 1.4$ L·h^{-1} and $\dot{m}_a = 450$, 520, 580, 700 and 900 kg·h^{-1}.

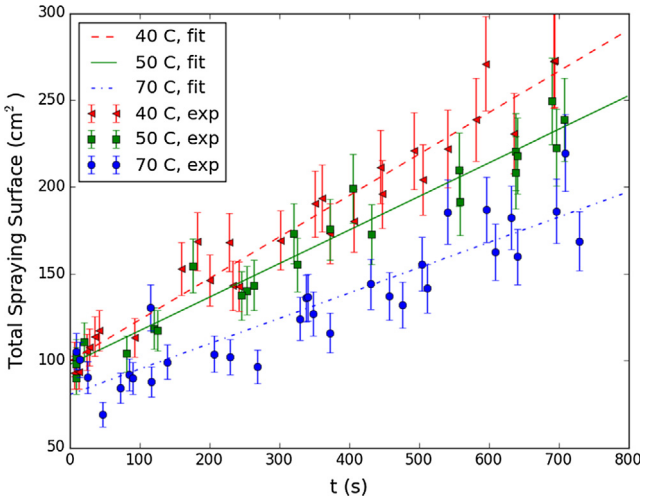

Fig. 10. Time evolution of the total spraying surface for at $T_i^{hex} = 40$, 50 and 70 °C, $\dot{m}_w^{hex} = 500$ L·h^{-1}, $\dot{m}_w^{nz} = 1.4$ L·h^{-1} and all $\dot{m}_a$ taken together.

3.3. Relation between heat transfer and impacted surface

With the correct definition of the impacted surface, a local ratio Γ has been introduced:

$$\Gamma = \frac{(1-\tau)\cdot \dot{m}_w^{nz}}{\rho_a v_a S_w^{nz,ce}} = \frac{1}{\mu_a}\cdot\left(\frac{\lambda_{Lo}}{Re_{\lambda_{Lo}}}\right)\cdot\left(\frac{(1-\tau)\cdot \dot{m}_w^{nz}}{S_w^{nz,ce}}\right) \quad (13)$$

This ratio Γ corresponds to the local water-to-air mass flux ratio, in other words the remaining sprayed water mass flux on the air mass flux related to the impacted surface scale. The evaporation rate τ was assumed to be 10% for all experiments [22]. This dimensionless number expresses also the interaction between airflow dynamics – with the Reynolds number – and the surface water flow.

In Fig. 12, this ratio is linked to the spraying efficiency of the second set of tests, for the three wall temperatures tested.

Fig. 12 shows the heat transfer is enhanced by a greater local ratio that is consistent with the literature [17,32]. Moreover, the heat transfer was higher at low wall temperature as the total spraying surface and the efficient cooling surface shown in Figs. 10 and 11. Thus, the heat transfer increases from 30% to 60% for 40 °C against

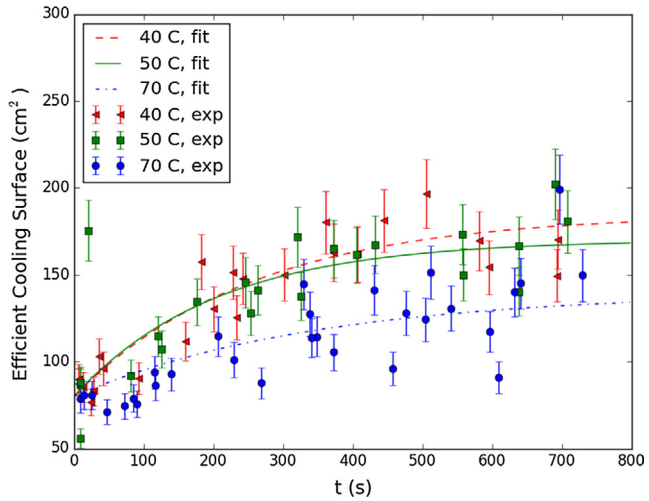

Fig. 11. Time evolution of the efficient cooling surface at $T_i^{hex} = 40$, 50 and 70 °C, $\dot{m}_w^{hex} = 500$ L·h^{-1}, $\dot{m}_w^{nz} = 1.4$ L·h^{-1} and all $\dot{m}_a$ taken together.

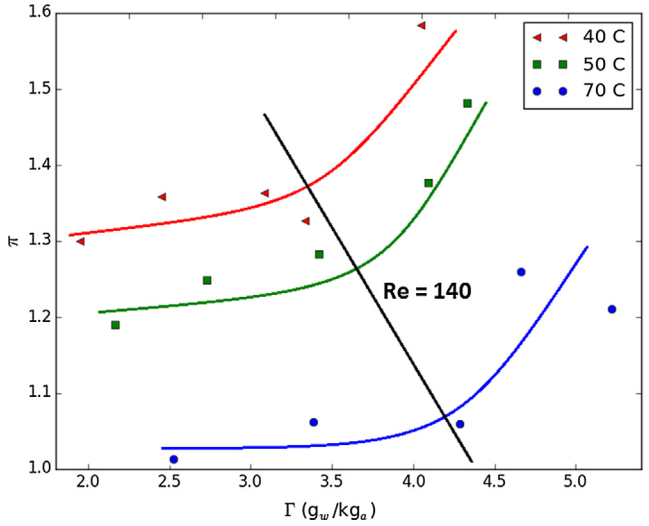

Fig. 12. Air-side spraying efficiency π vs water/air flow ratio Γ at $T_i^{hex} = 40$, 50 and 70 °C, $\dot{m}_w^{hex} = 500$ L·h^{-1}, $\dot{m}_w^{nz} = 1.4$ L·h^{-1}.

2% to 20% for 70 °C. Therefore, it can be noticed that the heat transfer depends on the wall temperature as well as the wet surface. Finally, the air-side spraying efficiency π displays two behaviors with the local mass flux. It grows slowly at low Γ and increases suddenly with a high Γ. This inflexion corresponds to a threshold value of the Reynolds number of about 140 below in which the spraying efficiency rises sharply and independently of the wall temperature.

By definition of local ratio Γ, the corresponding water mass flux on the impacted surface was deduced using Eq. (14) and a comparison can be done in similar manner.

$$\dot{m}_w'' = \frac{\Gamma \dot{m}_a}{S} \quad (14)$$

Thus, Table 5 shows that the present study obtained a heat transfer enhancement up to 160%, which is better than the results of Yang [15] and Chen [19] for similar water-to-air mass flux ratio but worth than the results of Tissot [18] and Zhang [17]. For Tissot, the spray is fine (droplets less than 25 μm) and injected in counter-flow. For Zhang, the spray is injected at 280 mm from the heat exchanger. These spraying conditions explain better heat transfer enhancements.

Table 5
Comparison with similar studies.

Authors	Air velocity ($m \cdot s^{-1}$)	Water mass flux ($kg \cdot m^{-2} \cdot h^{-1}$)	Water-to-air mass flux ratio ($g_w \cdot kg_a^{-1}$)	Heat transfer enhancement (%)
Yang and Clark [15]	0.93–13	39–83	13–29	113–145
Chen [19]	0.8–5.3	12.4–62	0.6–22	121–800
Present study	1.5–3	12–18	1.9–5.2	Up to 160
Tissot et al. [18]	1.1–2.2	12.4–18.7	1.3–3.9	Up to 300
hang et al. [17]	1.8–3.2	0.7–4.3	4.4–27	Up to 300

4. Conclusion & perspectives

In this paper, a system of water spraying with relative small amount of water (1–1.4 $L \cdot h^{-1}$) injected close to a heat exchanger surface (about 5 cm) was studied. A pilot has been built in order to control air and water flow rates, air temperature and humidity, as well as the atomizer position. The spray was not applied on the entire heat exchanger surface. The present work has showed that the heat transfer enhancement varies from 5 to 37%. A new method was developed to characterize the influence of the impacted surface for the best nozzle position. This method consists in an image analysis of infrared camera pictures of temperature distribution with and without spraying. Results reveal that two kinds of impacted surfaces could be considered because of different time evolution: the total spraying surface and the efficient cooling surface. The total spraying surface corresponds to the total frontal wet surface. The efficient cooling surface is the total spraying surface excluding the clogged parts. The efficient cooling surface is relevant to evaluate the efficiency of the spraying as this surface reaches a steady-state approximately at the same time than the heat transfer enhancement. It was found that these two surfaces are independent from the air flow rate but depend on the wall temperature. Thus, the efficient cooling surface represents 185 cm^2 at 40 °C compared to 140 cm^2 at 70 °C.I It drops with the wall temperature because of a higher evaporation rate. Subsequently, a local water-to-air mass ratio was determined. Finally, the spraying efficiency showed to increase with the water-to-air-mass ratio and decreases along with the wall temperature.

The present study of the impacted surface was focused on one atomizer in horizontal position. Further work need to be carried out on an atomizer in a vertical position to consider the gravity effect. Moreover, several atomizers should be used to cover a wider heat exchanger surface in order to evaluate whether there is a cumulative effect on the heat exchanger efficiency.

Acknowledgements

The authors are grateful for the financial support provided by the ADEME (Agence de l'Environnement et de la Maîtrise de l'Energie) in the context of the EfficAC project n°1482C0178. The authors also thank Renault and Valeo for lending them some equipment for their experiments.

Appendix A. Determination of the air-side heat transfer coefficient

In Eq. (8) shown again below, all the terms have to be determined to get the air-side heat transfer coefficient h_a.

$$\frac{1}{UA} = \frac{1}{\eta_a h_a n A_a^{hex}} + \frac{\delta_{Tu}}{k_{Al} A_a^{hex}} + \frac{1}{h_w A_w^{hex}}$$

First, the heat exchange surfaces on the air-side and on the water-side are:

- Inner surface: $A_w^{hex} = 2N_{Tu}N_{Ch}l_{hex}(s_{Ch} + l_{Ch})$
- Outer surface: $A_a^{hex} = A_{a,Fi}^{hex} + A_{a,Tu}^{hex} = \frac{2(N_{Tu}+1)l_{Fi}w_{Fi}l_{hex}}{\lambda_{Fi}} + 2N_{Tu}w_{Fi}l_{hex}$

δ_{Tu} is known from Table 1, A_a^{hex} is determined from equation above and the aluminum thermal conductivity value is fixed at 237 $W \cdot m^{-1} \cdot K^{-1}$. The conductive term is negligible compared to the two others terms: it is found to be less than 0.02% of the overall thermal resistance in all the experiments. Now, concerning the water-side convection term, it is the sum of the water-side convection in each of the four pass of the heat exchanger:

$$h_w A_w^{hex} = \sum_{b=1}^{4} h_{w,b} A_{w,b}^{hex} = A_w^{hex} \sum_{b=1}^{4} \frac{h_{w,b}}{N_{Ps,b}} = A_w^{hex}\left(\frac{h_{w,1}}{16} + \frac{h_{w,2}}{12} + \frac{h_{w,3}}{8} + \frac{h_{w,4}}{6}\right)$$

Each of these four water-side heat transfer coefficient are determined with the Nusselt number:

$$h_w^b = \frac{k_w}{Dh_w} Nu_w^b \tag{15}$$

The water flow in the minichannel can be either laminar or turbulent depending on the water-side Reynolds number value. This last one is given below with the water-side hydraulic diameter and the water side Prandtl number:

$$Pr_w = \frac{\mu_w Cp_w}{k_w}; \quad Dh_w = \frac{2s_{Ch}l_{Ch}}{s_{Ch} + l_{Ch}}; \quad Re_{Dh_w}^b = \frac{\dot{m}_w^{hex} Dh_w}{\mu_w N_b N_{Ch} s_{Ch} l_{Ch}}$$

With $N_b = [16, 12, 8, 6]$.

In laminar flow, the Nusselt number is expressed based on to the empirical relation established at boundary conditions of constant heat flux in [33]:

$$Nu_{lam} = \left\{ 4.354^3 + 0.6^3 + \left[1.953 \left(Re_{Dh_w} Pr_w \frac{}{l_{hex}} \right)^{\frac{1}{3}} - 0.6 \right]^3 + \left[0.924 P_w^{1/3} \left(\frac{Re_{Dh_w} Dh_w}{l_{hex}} \right)^{0.5} \right]^3 \right\}$$

In turbulent flow, an updated form of the Gnielinski equation [34] from [33] is used:

$$Nu_{turb} = \frac{(f/8) Re_{Dh_w} Pr_w}{1 + 12.7(f/8)^{1/2}(Pr_w^{2/3} - 1)} \cdot \left[1 + \left(\frac{Dh_w}{l_{hex}} \right)^{2/3} \right] \cdot \left[\frac{Pr_w(T = T_{wi}^{hex})}{Pr_w(T = T_{ai})} \right]^{0.11}$$

The transition between laminar flow and turbulent flow in flat tubes occurs at $Re_{Dh_w} = 2300$. However, this transition is not continuous. Gnielinski [33] proposed a linear interpolation to solve this problem and so the water-side Nusselt number used for this paper is expressed as follow:

$$\begin{cases} Nu = Nu_{lam}, 0 < Re_{Dh_w} < 2300 \\ Nu = (1-\gamma)Nu_{lam,2300} + \gamma Nu_{turb,4000}, 2300 \leqslant Re_{Dh_w} \leqslant 4000 \\ Nu = Nu_{turb}, 4000 < Re_{Dh_w} \end{cases}$$

With

$$\gamma = \frac{Re_{Dh_w} - 2300}{4000 - 2300} \quad and \quad 0 \leqslant \gamma \leqslant 1$$

For the friction factor f, it is not determined by the Konakov equation prescribed in [33]. Indeed, the value obtained with this equation is not in accordance with the standard values of the friction factor found in the literature. Instead, it is assumed that the friction factor is the same when the heat exchanger surface is dry or wet because of the low value of the sprayed water mass flow rate. This assumption is supported by the works of Chen and Zhang. Thus, the friction factor with the Chang correlation [28] is shown below:

$$f = f_1 \cdot f_2 \cdot f_3; \quad Re_{\lambda_{Lo}} = \frac{\rho_a v_a \lambda_{Lo}}{\mu_a} \tag{16}$$

$$f_1 = \begin{cases} 14.39 Re_{\lambda_{Lo}}^{-0.805\lambda_{Fi}/l_{Fi}} (\log_e(1.0 + (\lambda_{Fi}/\lambda_{Lo})))^{3.04}, & Re_{\lambda_{Lo}} < 150 \\ 4.97 Re_{\lambda_{Lo}}^{0.6049 - 1.064/\theta^2} (\log_e((\delta_{Fi}/\lambda_{Fi})^{0.5} + 0.9))^{-0.527}, & 150 < Re_{\lambda_{Lo}} < 5000 \end{cases}$$

$$f_2 = \begin{cases} (\log_e((\delta_{Fi}/\lambda_{Fi})^{0.48} + 0.9))^{-1.435} ((Dh_a/\lambda_{Lo}) \cdot \log_e(0.5 Re_{\lambda_{Lo}}))^{-3.01}, & Re_{\lambda_{Lo}} < 150 \\ ((Dh_a/\lambda_{Lo}) \cdot \log_e(0.3 Re_{\lambda_{Lo}}))^{-2.966} (\lambda_{Fi}/l_{Lo})^{-0.7931(\lambda_{Tu}/(\lambda_{Tu} - s_{Tu}))}, & 150 < Re_{\lambda_{Lo}} < 5000 \end{cases}$$

$$f_3 = \begin{cases} (\lambda_{Fi} w_{Fi}/l_{Lo}^2)^{-0.308} \exp(-0.1167 \cdot (\lambda_{Tu}/s_{Tu}))\theta^{0.35}, & Re_{\lambda_{Lo}} < 150 \\ (\lambda_{Tu}/s_{Tu})^{-0.0446} \log_e(1.2 + (\lambda_{Lo}/\lambda_{Fi})^{1.4})^{-3.553} \theta^{-0.477}, & 150 < Re_{\lambda_{Lo}} < 5000 \end{cases}$$

Finally, the water-side convection term is found to be between 14% and 28% of the overall thermal resistance for the first set of tests and between 1 and 7% for the second set of test: this difference is due to the heat exchanger water flow rate that changes from 200 $L \cdot h^{-1}$ to 500 $L \cdot h^{-1}$.

In the air-side convection term, the air-side surface efficiency η_a has to be determined. According to Zhang [17], this efficiency is expressed as:

$$\sigma_a = 1 - \frac{A_{a,Fi}^{hex}}{A_a^{hex}}(1 - \sigma_{Fi})$$

The fin efficiency is negligible compared to 1. So, $\sigma_a = A_{a,Tu}^{hex}/A_a^{hex}$. Finally, h_a is expressed as:

$$h_a = \left[\frac{A_{a,Tu}^{hex}}{UA} - \frac{\delta_{Tu}}{k_{Al}} \cdot \frac{A_{a,Tu}^{hex}}{A_a^{hex}} - \frac{Dh_w}{k_w} \cdot \frac{A_{a,Tu}^{hex}}{A_w^{hex}} \sum_{b=1}^{4} \frac{N_{Ps,b}}{Nu_w^b} \right]^{-1}$$

Appendix B. Flowchart of the experimental procedure

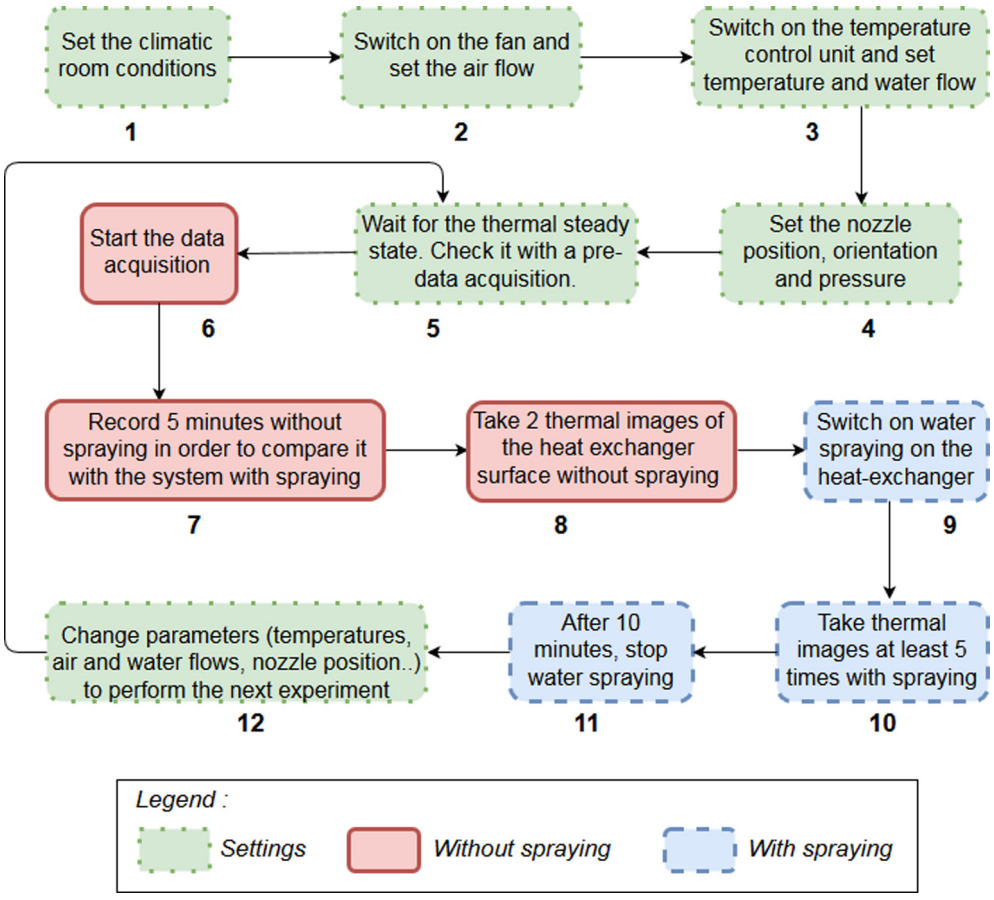
Set the climatic room conditions
1
Switch on the fan and set the air flow
2
Switch on the temperature control unit and set temperature and water flow
3
Set the nozzle position, orientation and pressure
4
Wait for the thermal steady state. Check it with a pre-data acquisition.
5
Start the data acquisition
6
Record 5 minutes without spraying in order to compare it with the system with spraying
7
Take 2 thermal images of the heat exchanger surface without spraying
8
Switch on water spraying on the heat-exchanger
9
Take thermal images at least 5 times with spraying
10
After 10 minutes, stop water spraying
11
Change parameters (temperatures, air and water flows, nozzle position..) to perform the next experiment
12
Legend :
Settings
Without spraying
With spraying

References

[1] J. Bollen et al., Co-Benefits of Climate Change Mitigation Policies: Literature Review and New Results, OECD Publishing, 2009.
[2] D.J. Arent et al., Key economic sectors and services, in: C.B. Field (Ed.), Climate Change 2014: Impacts, Adaptation, and Vulnerability. Part A: Global and Sectoral Aspects. Contribution of Working Group II to the Fifth Assessment Report of the Intergovernmental Panel of Climate Change, Cambridge University Press, Cambridge, United Kingdom and New York, NY, USA, 2014, pp. 659–708.
[3] M. Qi et al., Experimental research on water curtain diluting heavy gas dispersion in limited space with no ventilation, J. Loss Prev. Process Ind. 43 (2016) 471–478.
[4] A. Collin et al., Dynamics and thermal behaviour of water sprays, Int. J. Therm. Sci. 47 (4) (2008) 399–407.
[5] B. Basinger, G. Aguilar, J.S. Nelson, Effect of skin indentation on heat transfer during cryogen spray cooling, Lasers Surg. Med. 34 (2) (2004) 155–163.
[6] D. Tirawat et al., Combination of fogging and refrigeration for white asparagus preservation on vegetable stalls, Postharvest Biol. Technol. 124 (2017) 8–17.
[7] L. Lecoq, D. Flick, O. Laguerre, Study of the water evaporation rate on stainless steel plate in controlled conditions, Int. J. Therm. Sci. 111 (2017) 450–462.
[8] M. Hnizdil, P. Kotrbacek, Heat treatment of rails, Materiali in Tehnologije 51 (2) (2017) 329–332.
[9] W. Brown, Fundamental concepts integrating evaporative techniques in HVAC systems, ASHRAE Trans. 96 (Part 1) (1990) 1227–1235.
[10] R.O. Parker, The Heat, Mass Transfer Characteristics of an Evaporative Cooler, New York University, 1959, p. 127.
[11] I. Elperin, Heat transfer of two-phase flow with a bundle of tubes, Inzhererno Fizicheski Zhurnal 4 (8) (1961) 30–35.
[12] W. Nakayama, H. Kuwahara, S. Hirasawa, Heat-transfer from tube banks to air water mist flow, Int. J. Heat Mass Transf. 31 (2) (1988) 449–460.
[13] A.A. Dreyer, D.E. Kriel, P.J. Erens, Analysis of spray-cooled finned-tube heat-exchangers, Heat Transf. Eng. 13 (4) (1992) 53–71.
[14] A. Hasan, K. Siren, Performance investigation of plain and finned tube evaporatively cooled heat exchangers, Appl. Therm. Eng. 23 (3) (2003) 325–340.
[15] W.J. Yang, D.W. Clark, Spray cooling of air-cooled compact heat-exchangers, Int. J. Heat Mass Transf. 18 (2) (1975) 311–317.
[16] M. Youbi-Idrissi et al., Numerical model of sprayed air cooled condenser coupled to refrigerating system, Energy Convers. Manage. 48 (7) (2007) 1943–1951.
[17] F. Zhang et al., Simultaneous heat and mass transfer to air from a compact heat exchanger with water spray precooling and surface deluge cooling, Appl. Therm. Eng. 63 (2) (2014) 528–540.
[18] J. Tissot et al., Experimental study on air cooling by spray in the upstream flow of a heat exchanger, Int. J. Therm. Sci. 60 (2012) 23–31.
[19] C.W. Chen, C.Y. Yang, Y.T. Hu, Heat transfer enhancement of spray cooling on flat aluminum tube heat exchanger, Heat Transf. Eng. 34 (1) (2013) 29–36.
[20] A. Alkhedhair et al., Numerical simulation of water spray for pre-cooling of inlet air in natural draft dry cooling towers, Appl. Therm. Eng. 61 (2) (2013) 416–424.
[21] A. Lefebvre, Atomization and Sprays, CRC Press, 1988.
[22] P.E. Vende et al., Influence of position and orientation of water spraying on the efficiency of a heat exchanger, in: 4th International Conference on Contemporary Problems of Thermal Engineering (CPOTE), 2016. Katowice, Poland.
[23] J. Tissot et al., Air cooling by evaporating droplets in the upward flow of a condenser, Int. J. Therm. Sci. 50 (11) (2011) 2122–2131.
[24] R. Sureshkumar, S.R. Kale, P.L. Dhar, Heat and mass transfer processes between a water spray and ambient air – II. Simulations, Appl. Therm. Eng. 28 (5–6) (2008) 361–371.
[25] C.Q. Ren, H.X. Yang, An analytical model for the heat and mass transfer processes in indirect evaporative cooling with parallel/counter flow configurations, Int. J. Heat Mass Transf. 49 (3–4) (2006) 617–627.
[26] R.K. Shah, D.P. Sekulic, Fundamentals of Heat Exchanger Design, John Wiley & Sons, 2003, p. 941.
[27] W.M. Kays, A.L. London, Compact Heat Exchangers, third ed., McGraw-Hill, New York, NY, 1984.
[28] Y.J. Chang et al., A generalized friction correlation for louver fin geometry, Int. J. Heat Mass Transf. 43 (12) (2000) 2237–2243.
[29] A. Achaichia, T.A. Cowell, Heat-transfer and pressure-drop characteristics of flat tube and louvered plate fin surfaces, Exp. Therm. Fluid Sci. 1 (2) (1988) 147–157.
[30] P. Karthik, V. Kumaresan, R. Velraj, Fanning friction (f) and Colburn (j) factors of a louvered fin and flat tube compact heat exchanger, Therm. Sci. 21 (1) (2017) 141–150.
[31] P.W. Eckels, T.J. Rabas, Dehumidification - On the correlation of wet and dry transport processes in plate finned-tube heat-exchangers, J. Heat Transf. – Trans. Asme 109 (3) (1987) 575–582.
[32] B.A. Qureshi, S.M. Zubair, A comprehensive design and rating study of evaporative coolers and condensers. Part I. Performance evaluation, Int. J. Refrig 29 (4) (2006) 645–658.
[33] V. Gnielinski, On heat transfer in tubes, Int. J. Heat Mass Transf. 63 (2013) 134–140.
[34] V. Gnielinski, New equations for heat and mass-transfer in turbulent pipe and channel flow, Int. Chem. Eng. 16 (2) (1976) 359–368.